CASIE21-OBS: An Open-Access, OBS Controlled-Source Seismic Data Set for Investigating the Structure and Properties of the Cascadia Accretionary Wedge and the Downgoing Explorer-Juan de Fuca-Gorda Plate System

Juan Pablo Canales*[1], Nathaniel C. Miller[2], Wayne Baldwin[2], Suzanne M. Carbotte[3], Shuoshuo Han[4], Brian Boston[3,5], Hanchao Jian[1], John Collins[1], and Dan Lizarralde[1]

Abstract

Geological processes at subduction zones and their associated geohazards (e.g., megathrust earthquakes, submarine landslides, tsunamis, and arc volcanism) are, to a large extent, controlled by the structure, physical properties and fluid content of the subducting plate, the accreted sediments, and the overriding plate. In these settings, modern seismic modeling and imaging techniques based on controlled-source, multicomponent ocean-bottom seismometer (OBS) data are some of the best tools available for determining the subseafloor elastic properties, which can be linked to the aforementioned properties. Here, we present CASIE21-OBS, a controlled-source marine wide-angle OBS data set recently collected across the Cascadia convergent margin as part of the larger CAscadia Seismic Imaging Experiment 2021 (CASIE21). The main component of CASIE21 is a long-offset multichannel seismic (MCS) survey of the Cascadia margin conducted in June–July 2021 onboard R/V *M.G. Langseth* (cruise MGL2104) aiming to characterize the incoming plate, the plate interface geometry and properties, and the overlying sediment stratigraphy and physical properties. CASIE21-OBS was conducted during R/V *M.G. Langseth* cruise MGL2103 (May 2021) and R/V *Oceanus* cruise OC2106A (June–July 2021). It consisted of 63 short-period four-component OBSs deployed at a total 120 stations along 10 across-trench profiles extending from ~50 km seaward of the deformation front to the continental shelf, and from offshore northern Vancouver Island to offshore southern Oregon. The OBSs recorded the airgun signals of the CASIE21-MCS survey as well as natural seismicity occurring during the deployment period (24 May 2021 19:00 UTC–9 July 2021 09:00 UTC). The OBS data are archived and available at the Incorporated Research Institutions for Seismology Data Management Center under network code YR_2021 for continuous time series (miniSEED) and identifier 21-008 for assembled data set (SEG-Y).

Introduction

The potential for great megathrust earthquakes at subduction zones is influenced by a variety of factors, including the structure and properties of the incoming plate. For example, large-magnitude earthquakes ($M_w \geq 7.5$) are thought to occur preferentially

Cite this article as Canales, J. P., N. C. Miller, W. Baldwin, S. M. Carbotte, S. Han, B. Boston, H. Jian, J. Collins, and D. Lizarralde (2023). CASIE21-OBS: An Open-Access, OBS Controlled-Source Seismic Data Set for Investigating the Structure and Properties of the Cascadia Accretionary Wedge and the Downgoing Explorer-Juan de Fuca-Gorda Plate System, *Seismol. Res. Lett.* **XX**, 1–17, doi: 10.1785/0220230010.

Supplemental Material

---

1. Department of Geology and Geophysics, Woods Hole Oceanographic Institution, Woods Hole, Massachusetts, U.S.A., https://orcid.org/0000-0003-3066-7888 (JPC); https://orcid.org/0000-0002-8062-2082 (HJ); https://orcid.org/0000-0002-1040-7782 (JC); 2. Woods Hole Coastal and Marine Science Center, U.S. Geological Survey, Woods Hole, Massachusetts, U.S.A., https://orcid.org/0000-0003-3271-2929 (NCM); 3. Lamont–Doherty Earth Observatory, Columbia University, Palisades, New York, U.S.A., https://orcid.org/0000-0001-9471-700X (SMC); 4. Institute for Geophysics, University of Texas, Austin, Texas, U.S.A., https://orcid.org/0000-0002-2904-3659 (SH); 5. Now at Department of Geosciences, Auburn University, Auburn, Alabama, U.S.A.

*Corresponding author: jpcanales@whoi.edu

where thick incoming sediments contribute to a smooth plate interface, which favors rupture propagation (Heuret *et al.*, 2012; Scholl *et al.*, 2015; Seno, 2017; van Rijsingen *et al.*, 2018). Incoming sediment composition and physical properties also play a role in décollement development, extent of updip megathrust rupture, and potential for tsunamigenic slip to the trench (Dean *et al.*, 2010; Gulick *et al.*, 2011; Chester *et al.*, 2013; Geersen *et al.*, 2013; Hüpers *et al.*, 2017; Vannucchi *et al.*, 2017). Features characterizing the downgoing plate's crust and mantle such as seamounts, pseudofaults, and fracture zones represent hydration anomalies that may influence the seismogenic behavior of a subduction system. For example, pre- and postseismic activity in the M_w 8.3 Illapel, Chile, earthquake region was associated with hydrated slab structures (Poli *et al.*, 2017); the extent of bending-related faulting and inferred hydration off the Alaska Peninsula correlate with changes in incoming plate seismicity and deformation (Shillington *et al.*, 2015); and variations in pore-fluid pressure at the plate interface in the region of the 2010 M_w 8.8 Maule, Chile, earthquake, which are attributed to dehydration of a subducted fracture zone, may control the degree of interseismic locking and slip distribution of large earthquake ruptures (Moreno *et al.*, 2014).

The Cascadia convergent margin represents an end member of the global subduction zone system where the young, warm, and heavily sedimented Explorer-Juan de Fuca-Gorda oceanic plate system subducts beneath western North America (e.g., Wada and Wang, 2009; Fig. 1). Despite the lack of Cascadia megathrust events since 1700 and the generally low levels of instrumentally recorded plate interface seismicity (e.g., McCrory *et al.*, 2016), paleoseismology studies provide evidence for repeated subduction-related earthquakes and tsunamis in the past (e.g., Atwater, 1987; Goldfinger *et al.*, 2012; Walton *et al.*, 2021). The Cascadia margin shows along-strike changes in the thickness of incoming sediments (e.g., Hyndman *et al.*, 1990; Gulick *et al.*, 1998; Han *et al.*, 2018), crustal hydration (Horning *et al.*, 2016; Canales *et al.*, 2017; Boulahanis *et al.*, 2022), extent of plate-bending faulting (Han *et al.*, 2016), strength and consolidation state of accreted sediments and amount of sediment subduction (Gulick *et al.*, 1998; Han *et al.*, 2017; Peterson and Keranen, 2019), and presence of subducting seamounts (Tréhu *et al.*, 2012; Morton *et al.*, 2018) and mid-ocean-ridge-inherited propagator wakes (Wilson, 2002; Nedimović *et al.*, 2009). These variations in incoming plate and accretionary prism structure, together with along-strike changes in upper plate properties—including the variable location of the crystalline Siletzia terrain, which forms the backstop for the accretionary wedge, are thought to influence the along-strike variability of many of the properties of the Cascadia subduction zone (CSZ; e.g., Delph *et al.*, 2018), such as density of episodic tremor and slip (Brudzinski and Allen, 2007; Wech, 2010), plate interface locking (Schmalzle *et al.*, 2014), structural vergence (MacKay, 1995; Gulick *et al.*, 1998; Gutscher *et al.*, 2001; Adam *et al.*, 2004; Yelisetti *et al.*, 2017; Watt and Brothers, 2020), incoming plate and intermediate-depth seismicity (McCrory *et al.*, 2012; Stone *et al.*, 2018), and arc volcanic and geochemical segmentation (Schmidt *et al.*, 2008; Pitcher and Kent, 2019). Thus, advancing research on CSZ structure, processes, and geohazards requires comprehensive investigations of the structure and physical properties of the incoming and subducted Explorer-Juan de Fuca-Gorda plate system, as well as of the accretionary prism. Such investigations should systematically encompass the full length of the CSZ to adequately address the along-strike variability in structure and physical properties in Cascadia.

The CAscadia Seismic Imaging Experiment 2021 (CASIE21) ocean-bottom seismometer (OBS) deployment (hereinafter referred to as CASIE21-OBS) is a National Science Foundation (NSF-) and U.S. Geological Survey (USGS)-supported controlled-source marine seismic survey conducted offshore Cascadia in May–July 2021. The main goal of CASIE21-OBS was to collect a modern, open-access wide-angle seismic reflection and refraction data set that would enable scientists to develop *P*- and *S*-wave velocity models (V_P and V_S, respectively) of the structure of the accretionary prism and downgoing plate along most of the Cascadia margin between northern Vancouver Island and southern Oregon (Fig. 1). Such models will be ideally suited for, among other objectives: (1) documenting variations in accretionary wedge site response, which is critical for predicting shaking along the submarine Cascadia margin under hypothetical scenarios of future megathrust earthquake rupture. Variability in shaking properties may affect the distribution of slope failures, which influences tsunami hazard assessment (Gomberg, 2018). Understanding the variability in shaking properties along the Cascadia margin can also shed light onto proposed linkages between recurrence and rupture size of Cascadia paleo great earthquakes and the distribution of shaking-triggered turbidites (e.g., Goldfinger *et al.*, 2012, 2017), and the capacity for amplifying shaking from distant great earthquakes, potentially triggering small slope failures and turbidity currents (Johnson *et al.*, 2017). (2) Modeling the incoming and downgoing plate structure and extent of alteration, and their variability along the margin, which could help quantifying the contribution of downgoing plate structure (Horning *et al.*, 2016; Canales *et al.*, 2017; Boulahanis *et al.*, 2022) to the volcanic and geochemical segmentation of the Cascades arc (e.g., Schmidt *et al.*, 2008; Pitcher and Kent, 2019) and to other properties such as nonvolcanic tremor density (e.g., Wech, 2010), intermediate-depth seismicity (e.g., McCrory *et al.*, 2012), and fore-arc lower crustal velocity anomalies (Delph *et al.*, 2018). (3) Investigating potential relationships and links between accretionary wedge sediment physical properties (V_P, V_S, density, porosity, and fluid pore pressure), seafloor seepage (Johnson *et al.*, 2019), fluid migration through deep-seated fracture networks (Baumberger *et al.*, 2018), and variability in structural deformation style (landward vs. seaward) of the accretionary prism (e.g., MacKay, 1995; Johnson *et al.*, 2006; Han *et al.*, 2017).

CASIE21-OBS data were primarily collected along 10 trench-crossing 2D profiles (Fig. 1). Similar surveys have been conducted in the past in Cascadia (Flueh *et al.*, 1998; Parsons *et al.*, 1998; Gerdom *et al.*, 2000; Horning *et al.*, 2016; Canales *et al.*, 2017; Boulahanis *et al.*, 2022). However, one of the novelties of CASIE21-OBS is the quasi regular and close spacing of the primary 2D profiles along most of the length of the Cascadia margin, which will allow investigating along-strike variability in a systematic manner that had not been possible to date. Furthermore, recordings from out-of-plane profiles may be suitable for 3D modeling along some sections of the margin (Fig. 1). CASIE21-OBS leveraged and was conducted in coordination with the NSF-supported CASIE21-MCS (multichannel seismic), a long-offset MCS reflection survey of the Cascadia margin designed to provide regional-scale characterization of the offshore portion of the CSZ. Here, we present a description of these coordinated surveys and their scientific motivation and an overview of the CASIE21-OBS data quality, corrections, known issues, initial observations, and data availability. The intent of this publication is to promote and facilitate the use of this unique open-access data set by the larger geophysical community to advance research in CSZ structure, processes, and geohazards.

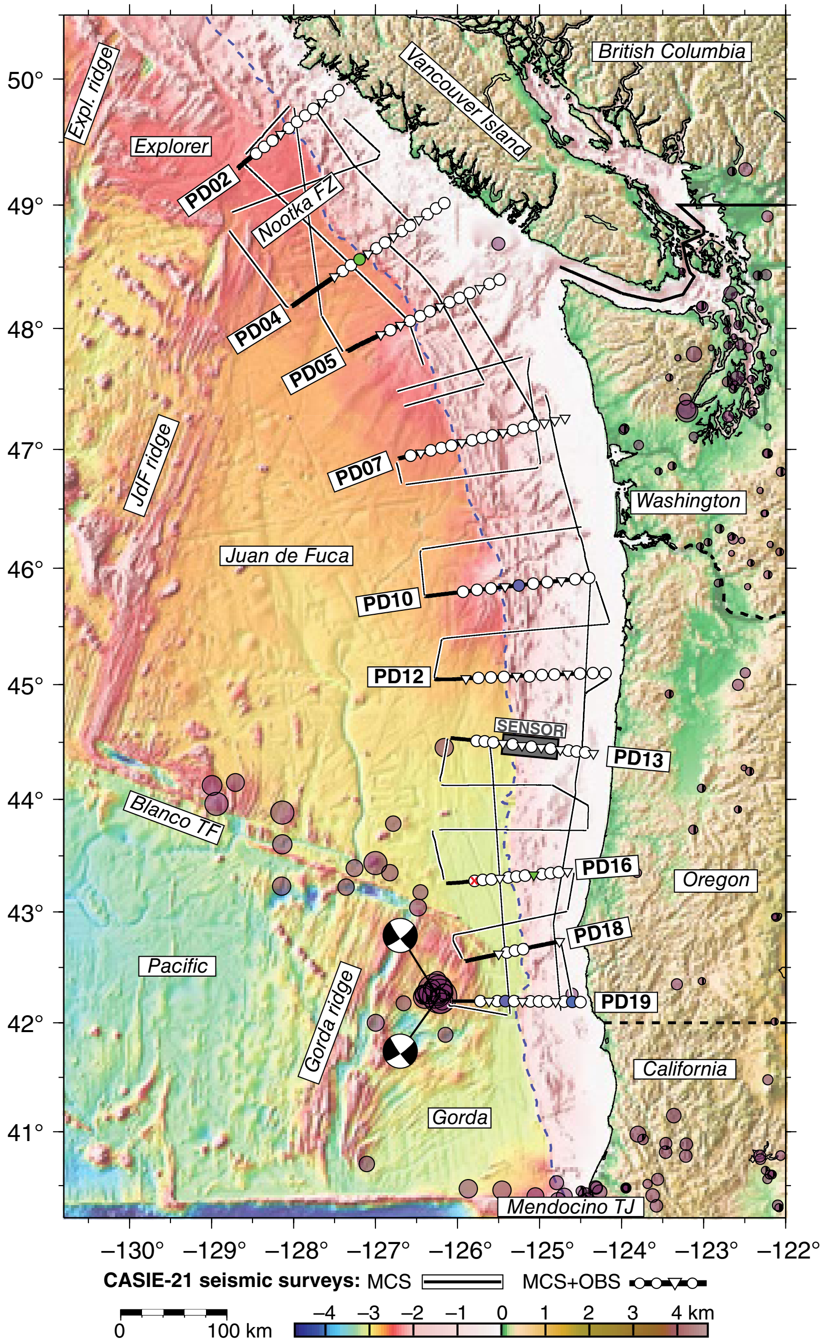

Figure 1. CAscadia Seismic Imaging Experiment 2021 multichannel seismic (CASIE21-MCS) and ocean-bottom seismometer (OBS) seismic surveys over bathymetry and elevation map of Cascadia basin, accretionary prism and subaerial fore-arc. Profiles aligned with 2D OBS arrays are labeled and shown in bold. Open symbols denote OBS locations: circles for Scripps Institution of Oceanography (SIO) LCs, inverted triangles for Woods Hole Oceanographic Institution (WHOI) D2s. Green OBSs on PD04 and PD16 correspond to sites S075 (Fig. 7) and S051 (Fig. 8), respectively. Blue OBSs on PD10 and PD19 correspond to sites S006 (Fig. 6e,f), S042 (Fig. 6c,d), and S034 (Fig. 6g,h). Red X on westernmost OBS on PD16 locates S044, which only returned ∼7% of data (supplemental material). Gray box at the center of PD13 locates the extent of the 2022 SENSOR array. Blue dashed line locates the Cascadia deformation front. Semitransparent purple symbols locate Advanced National Seismic System catalog seismicity (magnitude ≥1) during the duration of the CASIE21-OBS deployment (from 24 May 2021 19:00 UTC to 9 July 2021 09:00 UTC), sized according to magnitude. Focal mechanism plots mark epicenters and source mechanisms for the two 4 June 2021 M_{w} 5.9 Gorda plate events. The color version of this figure is available only in the electronic edition.

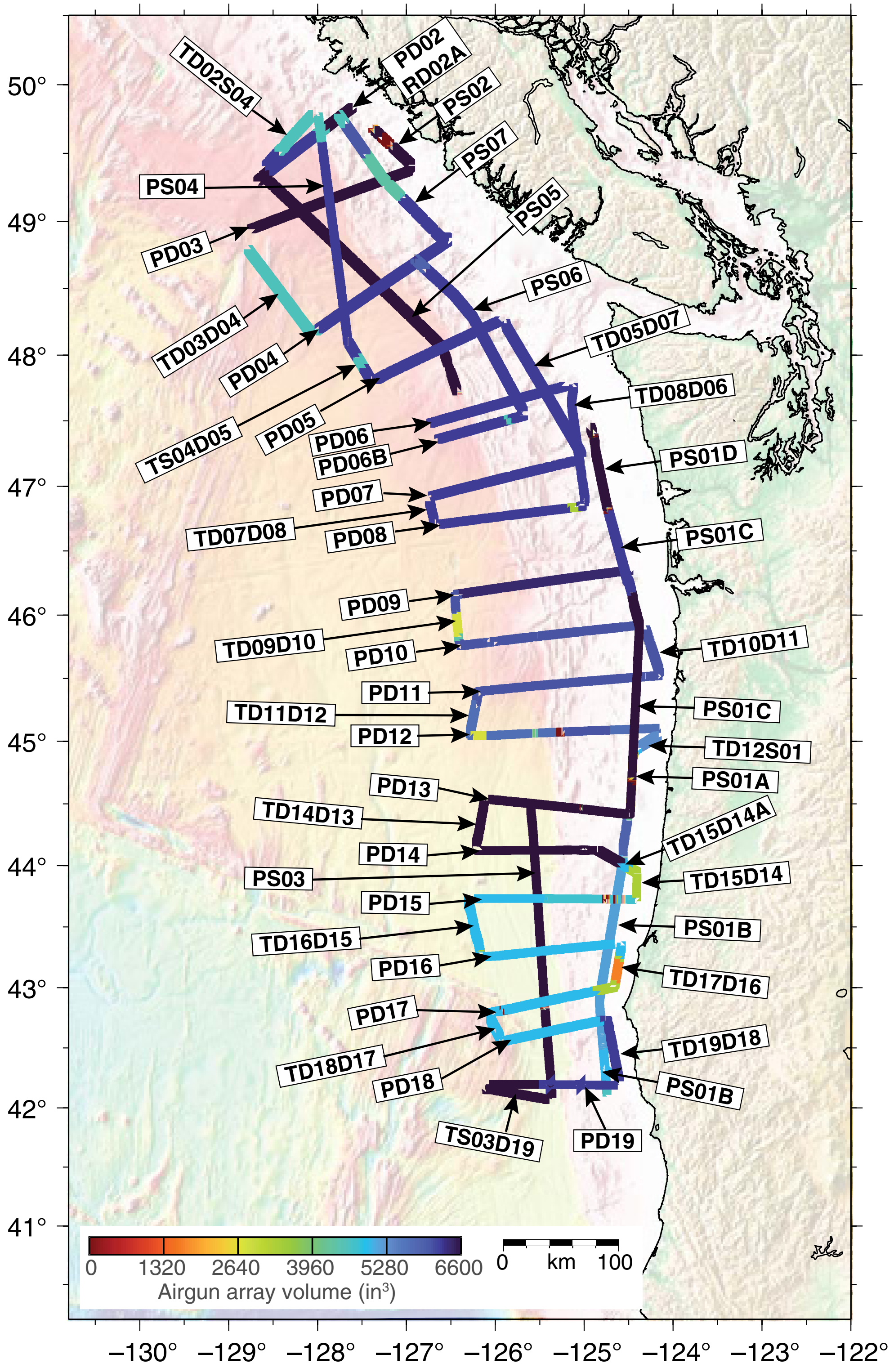

Figure 2. CASIE21-MCS profiles colored according to airgun array volume. Nomenclature key: D, dip line; P, primary; R, reshot; S, strike line; T, transit. (PD06B is considered a transit, not a primary profile despite its name.) During most of the survey, airgun array volume varied between 6600 in^3 (e.g., PD13), 6240 in^3 (e.g., PD05), 6060 in^3 (e.g., PD10), 4980 in^3 (e.g., PS01B), 4950 in^3 (e.g., PD18), and 4590 in^3 (e.g., TD03D04). Background is bathymetry and elevation as in Figure 1 shown semitransparent for clarity purposes. The color version of this figure is available only in the electronic edition.

Instrument Deployment and Details

Overview of CASIE21 experiments

CASIE21 is a multicomponent project aiming to acquire open-access marine seismic reflection and wide-angle seismic reflection and refraction data sets across the Cascadia accretionary wedge encompassing the full length of the margin, except the portion offshore northern California. The data sets consist of an MCS survey (Carbotte, Boston, and Han, 2022), an OBS survey to facilitate wide-angle reflection and refraction studies (this publication), and a more localized seafloor seismic nodal array for denser sampling in a particularly interesting region that will be published at a later date.

The primary component of CASIE is an ultra-long-offset MCS survey of the Cascadia margin (CASIE21-MCS), led by scientists from the Lamont–Doherty Earth Observatory (LDEO) of Columbia University, the University of Texas at Austin, and Woods Hole Oceanographic Institution (WHOI; Carbotte, Boston, and Han, 2022). CASIE21-MCS took place in June and July 2021 onboard *R/V Marcus G. Langseth* (cruise MGL2104) and collected ~5350 line km of MCS data using a 12–15-km-long hydrophone streamer and a 6600 in^3 airgun array (Fig. 2).

CASIE21-OBS consisted of 63 short-period OBSs each equipped with a three-component geophone and a hydrophone, deployed at a total of 120 stations located along 10 of the CASIE21-MCS dip profiles (Fig. 1). Deployments and recoveries were conducted in two cruises led by USGS personnel: *R/V M.G. Langseth* MGL2103 (May 2021) and *R/V Oceanus* cruise OC2106A (June–July 2021). The OBS instruments were provided and operated by the U.S. Ocean-Bottom Seismic Instrument Center (OBSIC). The primary goal of the OBS deployment was to increase the scientific return of the acoustic signals produced by the *R/V Langseth* airgun array during the CASIE21-MCS survey by acquiring a wide-angle seismic reflection and refraction data set that would enable investigations of the physical properties of the accretionary wedge, and structure and extent of alteration of the incoming and downgoing plates, among others. Reporting the CASIE21-OBS data set is the main objective of this publication.

The third component of CASIE21 is a high-resolution, controlled-source wide-angle survey conducted in April 2022 using a SEafloor Nodal Seismic array off ORegon (SENSOR) led by WHOI scientists onboard *R/V Langseth* (cruise MGL2201). CASIE22-SENSOR consisted of the deployment of a dense array of 107 short-period multicomponent (three-component geophone and a hydrophone) ocean-bottom nodes (OBNs) leased from Geospace Technologies. The OBNs were deployed at 500 m spacing along the central part of CASIE21-MCS dip line PD13 (Fig. 1) using a commercial remotely operated vehicle (ROV) from Pelagic Research Services. The OBNs recorded the signals from the *R/V Langseth* airgun array triggered every 75 m along a 2D profile coincident with PD13. The CASIE22-SENSOR data set is still undergoing quality controls and will be reported elsewhere.

In addition to these marine seismic surveys, an NSF- and USGS-supported complementary, temporary deployment of 862 onshore 5 Hz nodal seismometers along the southern Washington and Oregon Cascadia fore-arc also recorded the CASIE21-MCS airgun signals (Ward and Tréhu, 2020).

CASIE21-MCS experiment

CASIE21-MCS took place from 1 June to 11 July 2021, onboard *R/V M.G. Langseth* (cruise MGL2104), and acquired 2D MCS data along: (1) 18 primary dip profiles oriented perpendicular to the margin and spaced along the margin at 50–75 km intervals, (2) one multisegment strike profile along the Oregon, southern-central Washington, and central Vancouver Island continental shelf, and (3) two strike profiles ~6–10 km seaward from the deformation front offshore central-southern Oregon and Vancouver Island (Figs. 1, 2). In addition, 19 auxiliary profiles were collected while transiting between the main profiles, resulting in a total of 5347 line km of MCS data. The data were collected using a 15-km-long, 1200-channel hydrophone streamer during the first part of the survey (lines PD09, 10, 11, 12, and PS01A, B, and transits in between; Fig. 2), and with a 12-km-long, 960-channel hydrophone streamer during the rest of the survey. The airgun sources were towed at 12 m below the sea surface and triggered every 37.5 m, which corresponds to repetition rates of ~18.2–20.3 s when the ship was towing the 15-km-long streamer at speeds of 3.6–4.0 knots and ~15.5–16.2 s when the ship was towing the 12-km-long streamer at speeds of 4.5–4.7 knots. Most of the primary lines were shot with four airgun arrays with a total volume above 6000 in^3 at 2000 psi, although lines PD15, 16, 17, 18, and a large portion of PS01B were shot with three arrays with a total volume that varied between 4730 and 4950 in^3 (Fig. 2) because rough weather conditions prohibited getting a misfunctioning gun array on deck for repairs (Carbotte *et al.*, 2021). A number of other airgun array volume changes occurred throughout the survey due to technical issues and in response to marine mammal and other wildlife mitigation procedures (i.e., source shutdowns and rump-ups; Table S1, available in the supplemental material to this article).

CASIE21-OBS experiment

OBS instrumentation. CASIE21-OBS used a total of 63 OBS instruments from OBSIC. About 45 of the instruments were provided and operated by the Scripps Institution of Oceanography (SIO); the other 18 instruments were provided and operated by the WHOI. The SIO instruments were "LC4 × 4" (low-cost [LC]) short-period OBSs, which record velocity data from three-component (vertical and two horizontal) Sercel L-28 4.5 Hz geophones and pressure data from a High Tech HTI-90-U hydrophone on an SIO-designed LC4 × 4 24-bit digitizer, with timing provided by a Seascan digitally temperature-compensated crystal oscillator (DTCXO). The WHOI instruments were "D2" short-period OBSs, which carry three-component Geospace GS-11D 4.5 Hz geophones and High Tech HTI-90-U hydrophone, recorded by a Quanterra Q330 datalogger with timing from a Seascan DTCXO clock. All instruments were programmed to record at 200 Hz. Clocks were synchronized to Global Positioning System time before deployments and after recovery, which allows for a linear clock drift correction.

Cruise activities. *R/V Langseth* cruise MGL2103 departed Newport, Oregon, on 24 May 2021, for the initial deployment of OBSs offshore Oregon. *Langseth* deployed 60 of the 63 available OBSs along lines PD10, PD12, PD13, PD18, and PD19 (Fig. 1) and returned to Newport, Oregon, on 28 May 2021. *Langseth* then returned to sea on cruise MGL2104 on 1 June 2021 to start airgun and streamer operations.

The original experiment plan included deployment of densely spaced OBNs along the central portions of lines PD10, PD13, and PD18. These deployments were attempted by ROV from 23 to 31 May 2021, on *R/V Oceanus* cruise OC2105A, but technical problems led to cancelation of the original OBN component. (The OBN experiment was reattempted and successfully completed along line PD13 in April 2022 by the CASIE22-SENSOR project; see the Overview of CASIE21 experiments section.) The decision to cancel OC2105A was made while MGL2103 was still at sea, which allowed planned OBS sites to be redistributed to fill the OBN section of PD10.

A second *R/V Oceanus* leg—cruise OC2106A—was tasked with recovering 57 of the 60 OBSs deployed by *Langseth* and redeploying 60 instruments farther north. Because of the shortened OBN leg (OC2105A), *Oceanus* was able to depart earlier than planned on OC2106A from Newport, Oregon, on 19 June 2021. The extra time allowed *Oceanus* to recover four instruments from the seaward end of PD12 and deploy a total of six instruments to fill the OBN portion of PD13 prior to *Langseth* shooting PD13. However, the OBN portion of PD18 could not be filled, thus resulting in an OBS distribution gap of ∼37 km along PD18 between sites S059 and S060 (Fig. 1, Table S2). After filling in PD13 and waiting for *Langseth* to complete shooting each line, *Oceanus* recovered all OBSs from lines PD16, PD18, PD19, and PD13 offshore Oregon. Then, *Oceanus* moved north to deploy OBS on lines PD02, PD04, and PD05. Next, *Oceanus* recovered the remaining instruments on PD12 and PD10 and deployed on PD07. As *Langseth* completed shooting the northern lines, *Oceanus* finally recovered OBS from lines PD02, PD04, PD05, and PD07 and ended OC2106A in Port Angeles, Washington, on 11 July 2021. A detailed list of deployment and recovery times and locations for all OBS sites is included in Table S2. The OBS recording period, from the first deployment of cruise MGL2103 to the last recovery of cruise OC2106A, was from 24 May 2021 19:00 UTC to 9 July 2021 09:00 UTC.

Data Quality and Availability

The CASIE21-OBS data set complies with the Memorandum of Agreement between the U.S. Navy and the NSF for Ocean Observing System Security. Immediately after data collection, the data set was sent to the U.S. Navy's Commander Undersea Surveillance for screening, and redacted if deemed appropriate. The redacted data set was returned to OBSIC and the PIs in December 2021. Of the WHOI OBS data, a total of 57,408 data-hours (four channels) were screened, and 0.2% of them redacted. Of the SIO OBS data, a total of 167,424 data-hours (four channels) were screened, and 0.12% of them redacted. Archived data (see Data and Resources) and data descriptions in this publication all refer to the screened and redacted data set.

Instrument and data problems

LC ID 305 deployed at station S044 on PD16 (Fig. 1) was recovered with a flooded data logger, returning only ∼7% of the expected data volume. SEG-Y data for lines PD09, PD10, TD09D10, and TD10D11 are the only data available from this instrument. LC ID 302 (station S053) also returned with a wet data logger, but all data were intact and recoverable. Because of the wet data loggers in these two OBSs, no time synchronization could be done after recovery. Therefore, the data from these two instruments have not been corrected for clock drift.

Data quality control revealed the presence of data gaps (i.e., missing or excess samples) in some of the segments in the miniSEED data files from two of the SIO LC instruments: LC ID 56 (deployed at stations S002 and S110) and LC ID 224 (deployed at station S058; Table S5). The origin of these data gaps seems to be related to faulty hardware in the instruments, not to data extraction and transcription. These data gaps, if left uncorrected, result in SEG-Y receiver gathers with timing errors, as evidenced by near-offset direct water waves arriving too early (even at negative times) when compared to predicted travel times (Fig. S1a,c), and by abrupt time shifts (Fig. S1a). Detailed inspection of data from these instruments indicates that for data segments with sample gaps, the time stamp of the first sample in the segment is correct, but the time stamp of the last sample in the segment is offset by the number of missing samples. We cannot assess how the time misfit varies from the first to the last sample in the miniSEED segment, but it is reasonable to assume that the variation in time misfit is linear along the data segment. With this assumption, we have created gap-corrected SEG-Y files for stations S002, S058, and S110. The corrected data match pretty well with the predicted direct water wave arrivals, and the abrupt time shifts are eliminated (Fig. S1b,d). Thus, we are confident that our correction for the miniSEED data gaps is accurate. Assembled data (SEG-Y) available at the Incorporated Research Institutions for Seismology Data Management Center (IRIS-DMC) for stations 002, 058, and 110 include these corrections. However, for the sake of preserving the original data, the continuous data in miniSEED format are archived uncorrected.

Instrument relocation

The OBSs were dropped over the side of the ship and left to sink to the seafloor. No acoustic ranging surveys were conducted to interrogate the OBSs and triangulate their positions during deployment or prior to recovery (e.g., Russell *et al.*, 2019). Determination of their final positions on the seafloor was achieved by instrument relocation using the observed travel times of direct waves for shot-receiver offsets ≤3 km. We conducted an iterative grid-search method to find a relocated position that minimizes the difference between predicted and observed travel times (Δt). We first made an initial estimate of the average water sound speed by least-squares fitting the direct wave travel times as a function of distance from sources to the initial drop location. We then conducted a grid search of points on the seafloor regularly spaced every 1 m within a 500-m-radius search area to find the location that resulted in the minimum Δt. Depths were taken from the multibeam bathymetry data collected during cruise MGL2104. We then repeated the estimation of the water sound speed using the new relocated position and conducted a new grid search. These steps were repeated iteratively until the root mean square of Δt did not decrease significantly anymore; five iterations were typically sufficient. An error ellipse was estimated at each relocated position

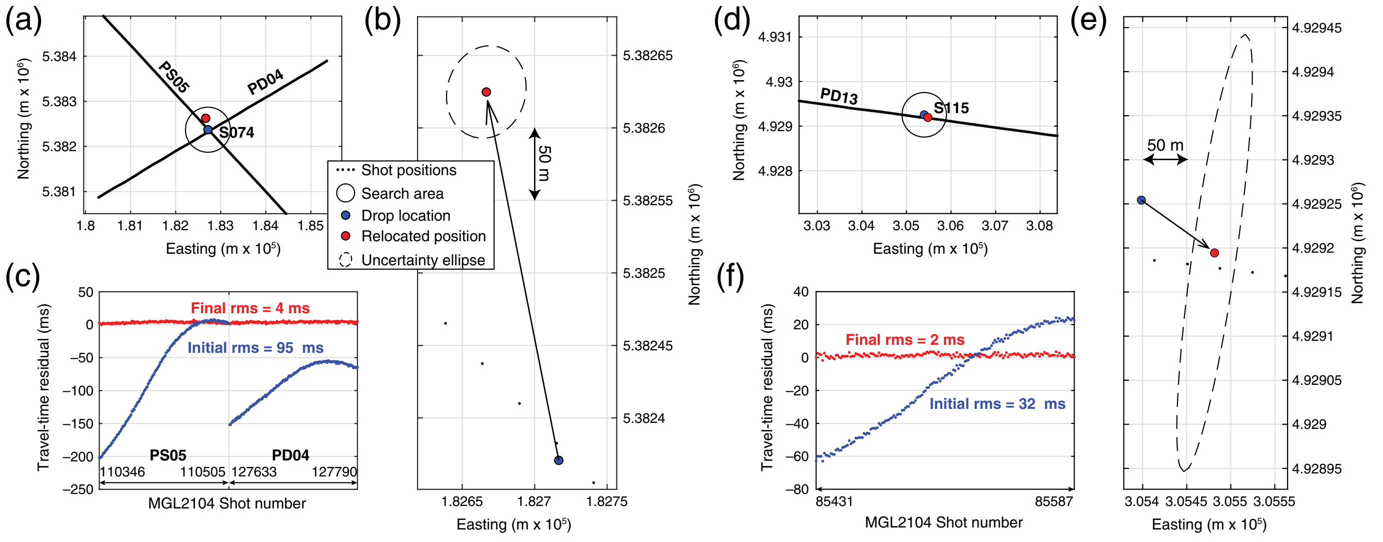

Figure 3. Example of instrument relocation for station 074. (a) Map view of locations of shots used in the relocation, the 500-m-radius search area, and drop and relocated positions of the instrument. (b) Zoomed-in version of panel (a) showing the uncertainty ellipse around the relocated position. (c) Residual travel times of direct wave arrivals for the drop (initial) and the relocated (final) positions. (d–f) Same as (a–c), respectively, for station 115. The color version of this figure is available only in the electronic edition.

by selecting all grid-search positions that resulted in travel-time residuals with $\chi^2 \leq 1$, accounting for uncertainties in travel-time picks (5 ms) and shot locations (5 m). Figure 3 shows two examples of the relocation results. In the few cases for which OBSs were located near crossing profiles with different azimuth, relocated position uncertainties are small (Fig. 3a–c), but in the majority of cases for which OBSs were located near only one shooting profile, uncertainties in the direction orthogonal to the shooting profile are larger (Fig. 3d–f).

Drop and relocated positions, as well as their uncertainty estimates, are listed in Table S2. For the majority of instruments, relocated positions are within ∼40–120 m from the drop location (Fig. 4). For instruments for which there were no shots within 3 km of the drop location, no relocation has been attempted. In these cases, the relocated position reported in Table S2 corresponds to the drop location, which is assumed to be accurate enough as most of these instruments were located in shallow water on the continental shelf. Only two instruments in deeper water could not be relocated: station S015 on PD12 because of airgun shutdowns in its vicinity (Fig. 2, Table S1), and station S044 on PD16 because of partial data recovery (see the Instrument and data problems section).

Instrument orientation

Orientation of the geophone horizontal components has been estimated using the method described in Anderson *et al.* (1987) and Duennebier *et al.* (1987). Figure 5 illustrates the procedure using site 107 as an example. First, the angle to rotate data from channels EL1 and EL2 to radial and transverse components was calculated by linear fitting the particle motion hodograms of channel EL1 versus EL2 measured in a 120 ms time window starting 20 ms before the direct wave arrivals for traces within 20 km shot-receiver offsets (Fig. 5e,f). For each instrument, the orientation of EL1 (α) was derived by subtracting the back azimuth θ (Fig. 5d) from the estimated EL1-to-radial rotation angle (Fig. 5g), and averaging across offsets after excluding outliers and data points for very near offsets (<0.75 times instrument depth) for which the back azimuth is highly sensitive to the uncertainties in instrument location (Fig. 5j). Orientation results were then validated by transforming EL1 and EL2 channels into radial and transverse components (Fig. 5h,i) and inspecting the ratio between radial and transverse component amplitudes (Fig. 5l) as well as the polarity of the radial component

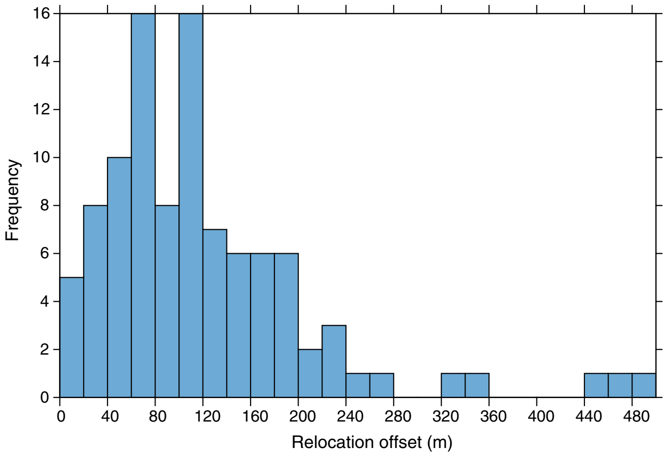

Figure 4. Histogram of instrument relocation offsets (lateral distance between drop and relocated positions). The color version of this figure is available only in the electronic edition.

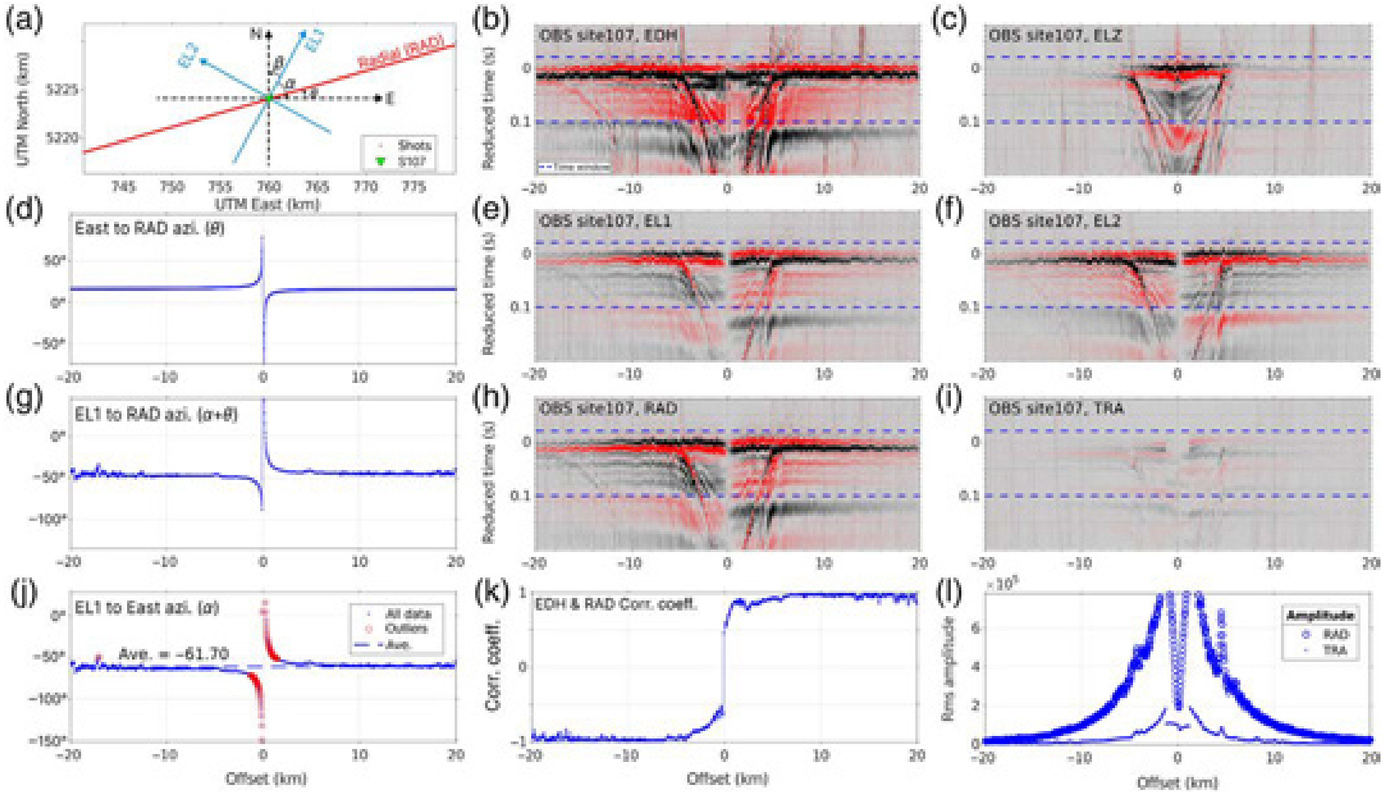

relative to that of the hydrophone. The polarity was defined using the cross-correlation coefficients between the hydrophone and radial geophone components (Fig. 5k), following a convention that the coefficients should be negative or positive for shots located to the west or east, respectively, of the OBS. In the instances where the opposite pattern was observed, we corrected the EL1 orientation by 180° or −180° to ensure that $\alpha \in [-180°, 180°]$.

We report OBS orientation as the angle α that rotates channel EL1 to east, with positive values indicating counterclockwise rotation from EL1 to east (Table S2). CASIE21-OBS data users may test other methods for estimating instrument orientation, as using arrivals from other acoustic sources (Trabattoni *et al.*, 2020), or from low-frequency Rayleigh waves (Stachnik *et al.*, 2012; Zha *et al.*, 2013; Janiszewski and Abers, 2015; Doran and Laske, 2017).

Power spectra

We use IRIS MUSTANG service (Casey *et al.*, 2018) to obtain power spectral density (PSD) estimates of the data set at each station. Figure 6a,b shows average median PSD estimates in 1-hr-long records for the full duration of the deployment for each station. At long periods (0.02–0.1 Hz), the shallowest instruments (~<500 m) show significant noise levels in all geophone channels, whereas deeper instruments have lower noise levels in this band. The microseismic peak (0.1–2 Hz) shows a similar pattern for the vertical channels but is less clear for the horizontal channels. The higher noise levels for long periods for shallow instruments are probably due to the "surf beat," which is long-period energy trapped within 1 km of the coastline into waveguides formed by the sloping bathymetry (Webb, 1998). At short periods (>2 Hz), there is no clear dependence on instrument depth of the PSD when averaged for the full duration of the experiment.

Figure 5. Determination of horizontal components' orientation for site 107 on line PD07. (a) Map view of site 107, shots along PD07 within 20 km offset and the local coordinate system centered at site 107. Right-handed convention (positive angles for counterclockwise rotation) is assumed in the analysis. (b,c,e,f) show the band-pass filtered (4–60 Hz) direct arrival data in hydrophone (EDH), vertical (ELZ), and two horizontal (EL1 and EL2) geophone components, respectively. (d) The radial direction with respect to east (back azimuth θ in panel a, $\theta \in [-90°, 90°]$). (g) The rotation angle from EL1 to radial (estimated by linear fitting of the EL1 and EL2 particle motion hodogram) rendered to [−90°, 90°], which is equivalent to $\alpha + \theta$ as shown in panel (a). (h,i) Rotated radial (RAD) and transverse (TRA) components. (j) The angle between channel EL1 and east (α in panel a, $\alpha \in [-180°, 180°]$) is calculated by subtracting data in panel (d) from data in panel (g) and averaging across offsets after removing outliers. (k) Cross-correlation coefficients between the hydrophone and radial components, used for polarity check and correction. We follow a convention where the coefficient is negative or positive at negative or positive offsets, respectively. (l) Comparison of root mean square amplitude of the radial and transverse components. The color version of this figure is available only in the electronic edition.

To illustrate the PSD of the data set during the periods of airgun activities, we show PSD estimates for three instruments located in shallow (S042, Fig. 5c,d), intermediate (S006, Fig. 5e,

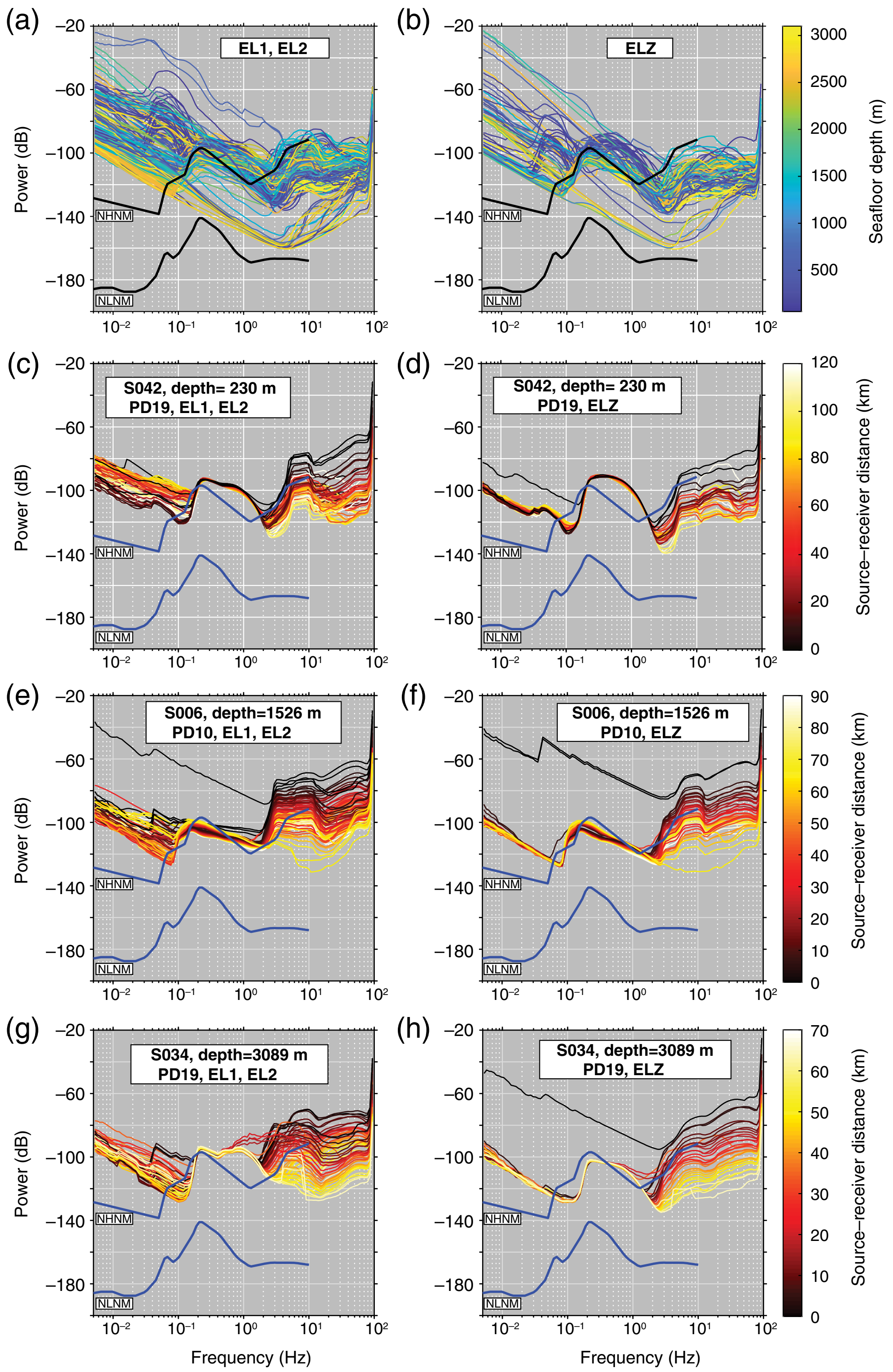

Figure 6. Power spectral density (PSD) estimates. (a,b) Median PSD for all stations during the full duration of the CASIE21-OBS deployment for horizontal and vertical channels. PSD curves are colored according to seafloor depth. (c,d) Example of PSD for a station located in shallow water (230 m) during the period of airgun activities along the MGL2104 profile coincident with the OBS location for horizontal and vertical channels. PSD curves are colored according to lateral distance between source array and OBS. (e,f) Same as panels (c,d) for an OBS located in intermediate-depth water (1526 m). (g,h) Same as panels (c,d) for an OBS located in deep water (3089 m). Bold curves show the "new high- and low-noise models" (NHNM and NLNM, respectively) of Peterson (1993). The color version of this figure is available only in the electronic edition.

f), and deep water (S034, Fig. 5g,h) from data recorded while airgun shooting along the profiles over these stations. As expected, PSD levels at short periods show a clear dependence with distance from the instrument to the airgun array.

Data formats

After extraction from the datalogger, the data were reformatted as continuous time series in miniSEED format (International Federation of Digital Seismograph Networks [FDSN], 2012). Data from each station and channel are split across miniSEED files each containing 1-day-long records. Filenames for data downloadable from the IRIS-DMC (see Data and Resources) for SIO and WHOI instruments are as following, respectively: *STAT*.*CHA*.2021.*DAY*.00.59.59.msd and YR_*STAT*_*CHA*__2021_*DAY*.msd, in which *STAT* is a four-character station identifier (e.g., S001, S002, …, S120), *CHA* is a three-character channel identifier (EL1, EL2, ELZ, or EDH), and *DAY* corresponds to three-digit Julian day.

As is standard for controlled-source seismic data sets, the continuous time series have been cut into SEG-Y receiver gathers to facilitate phase identification and travel-time picking. Data from each station, channel, and airgun shooting transect (Fig. 2) were gathered into receiver gather files containing 90-s-long traces. File nomenclature for the SEG-Y data downloadable from the IRIS-DMC (see Data and Resources) is as follows: MGL2104*LINE*_*STAT*_*CHA*.segy, in which *LINE* is the identifier of the MGL2104 airgun profiles (Fig. 2, Table S3). The SEG-Y files contain most of the standard trace headers (Table S4).

As is standard practice, instrument response corrections have not been applied to either the continuous miniSEED or cut SEG-Y data. Nominal responses for the SIO and WHOI instruments are included in StationXML format with the continuous data archive.

Initial Observations

Controlled-source data

The primary technical goal of the CASIE21-OBS deployment was for the OBSs to record the MGL2104 airgun signals along the collocated profiles, and this was accomplished for 119 of 120 deployments (see the Instrument and data problems section). Although the rapid shot interval resulted in significant previous-shot noise (Nakamura *et al.*, 1987; Christeson *et al.*, 1996), the receiver gathers display very good quality data with clearly identifiable sedimentary, crustal, and mantle arrivals (Figs. 7, 8). These include *P*-wave refractions such as *Pg* and *Pn* and reflections from the igneous basement and the Moho (P_mP) (Figs. 7b,c and 8b,c). These data are particularly well suited for modeling the V_P structure of the oceanic plate down to the upper mantle prior to subduction and below the offshore fore-arc, as well as of the accretionary prism and continental shelf. The regular and close spacing of the primary profiles along most of the length of the Cascadia margin as well as the spacing of instruments along these profiles are a first-order improvement relative to similar past surveys (Flueh *et al.*, 1998; Parsons *et al.*, 1998; Gerdom *et al.*, 2000; Horning *et al.*, 2016; Canales *et al.*, 2017; Boulahanis *et al.*, 2022). In addition to recording data from the collocated profiles, the OBS deployments were long enough such that the OBSs also recorded shots from many offline profiles. This will enable studies of the 3D architecture in some sections of the margin. This data set will enable researchers to investigate subduction zone processes occurring between the deformation front and the coast with unprecedented detail systematically along the margin. Crustal-scale seismic velocity models along the Cascadia margin will enable investigations of links between incoming plate variability and a number of CSZ properties (e.g., Delph *et al.*, 2018), such as density of episodic tremor and slip (Brudzinski and Allen, 2007; Wech, 2010), plate interface locking (Schmalzle *et al.*, 2014), structural vergence (MacKay, 1995; Gulick *et al.*, 1998; Gutscher *et al.*, 2001; Adam *et al.*, 2004; Yelisetti *et al.*, 2017), intermediate-depth seismicity (McCrory *et al.*, 2012; Stone *et al.*, 2018), and arc volcanic and geochemical segmentation (Schmidt *et al.*, 2008; Pitcher and Kent, 2019).

The data also contain arrivals from *S*-converted waves, such as *PSS* and *PPS* modes (*P*-to-*S* conversions at the basement on the downgoing and upgoing paths, respectively) (Figs. 7d, 8d). These arrivals will help constrain the V_S structure of the incoming and accreted sediments and of the oceanic crust and mantle (Kumar *et al.*, 2007; Peacock *et al.*, 2010; Dash and Spence, 2011; Tsuji *et al.*, 2011; Zhu *et al.*, 2020). V_P and V_S models will allow investigating physical properties such porosity and fluid pore pressure, which can be related to basal sediment consolidation and fluid expulsion and/or retention (e.g., Han *et al.*, 2017), fluid drainage structures and their relation to wedge structural style (e.g., seaward vs. landward thrusting) and observations of seafloor fluid seepage (e.g., Johnson *et al.*, 2006, 2019; Baumberger *et al.*, 2018). For example, data from OBS S075 located a few kilometers seaward from the deformation front (Fig. 7a) show clear *Sg*, S_mS, and *Sn* arrivals from shots located to the west of the instrument but not for shots located over the wedge slope (Fig. 7d), suggesting that the physical properties at the plate boundary (the likely interface for efficient *P*-to-*S* conversion) vary across the deformation front (e.g., Peterson and Keranen, 2019).

Seismicity

Although the CASIE21-OBS was primarily a controlled-source experiment, the instruments also recorded the natural seismicity during the period of the deployment (24 May 2021 19:00 UTC to 9 July 2021 09:00 UTC). The USGS National Earthquake Information Center indicates that seismicity during this time period was concentrated along the Blanco transform fault, the Mendocino triple junction, the Cascadia fore-arc with predominance beneath western Washington, and the interior of the Gorda plate (Fig. 1). In the latter region, two M_w 5.9 events took place on 4 June 2021, at 07:52 UTC and 08:17 UTC at 14–17 km depth, with a series of aftershocks occurring in the nearby region during the following 13 days (Fig. 1). The OBSs of the first CASIE21-OBS deployment (cruise MGL2103, see the Cruise activities section)—that is, those located along the profiles on the Oregon margin PD10, PD12, PD13, PD16, PD18, and PD19—were deployed prior to, and recovered after, this sequence of Gorda events and, therefore, recorded these earthquakes and their aftershocks (Fig. 9).

Records of natural seismicity registered in the CASIE21 OBSs will expand existing regional seismic catalogs developed from previous OBS deployments (e.g., Morton *et al.*, 2018; Stone *et al.*, 2018), and can be used for a variety of studies including seismicity of the plate interface (e.g., Gong and McGuire, 2018; Alongi *et al.*, 2021) and oceanic plate structure (e.g., VanderBeek and Toomey, 2019). The data set will also allow researchers to investigate variability in seafloor shaking attributes (i.e., site response) both along the margin as well as across the accretionary prism (Gomberg, 2018). Such information is critical for predicting shaking offshore the western United States under hypothetical scenarios of future megathrust earthquake rupture, for assessing tsunami hazards due to megathrust earthquakes and associated submarine landslides, and to test proposed linkages between paleo great earthquakes and distribution of shaking-triggered turbidites (Johnson *et al.*, 2017; Priest *et al.*, 2017; Gomberg, 2018).

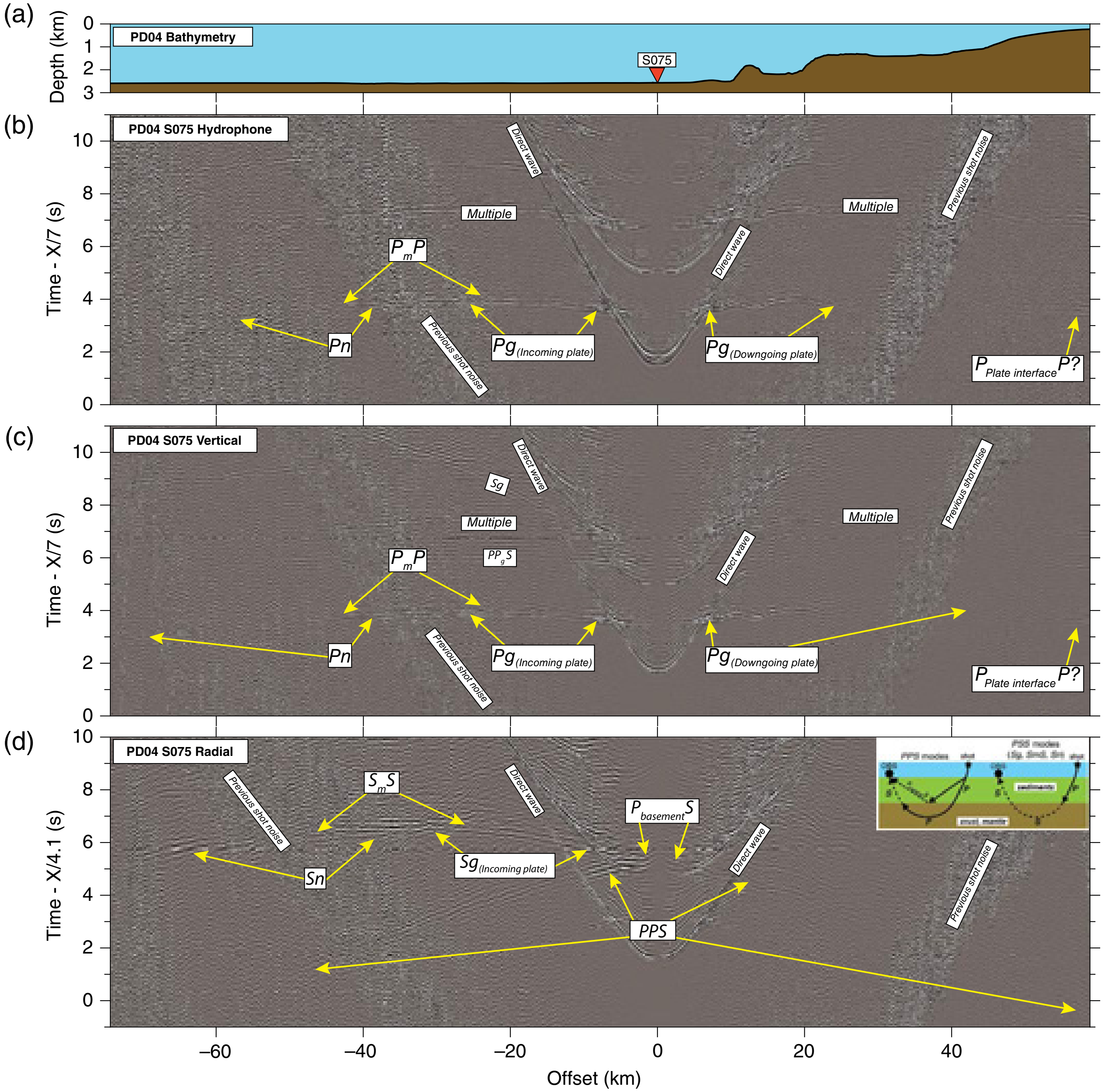

Figure 7. Receiver gathers from instrument S075 located on the abyssal plain near the Cascadia deformation front on profile PD04 (see location in Fig. 1). Data are band-pass filtered (3–5–20–25 Hz). (a) Bathymetry along profile. (b) Hydrophone channel EDH, with time reduced by 7 km/s. (c) Vertical channel ELZ, with time reduced by 7 km/s. (d) Radial component obtained from rotating horizontal channels EL1 and EL2, with time reduced by 4.1 km/s. Main refracted and reflected phases are labeled. Inset in panel (d) shows schematic ray paths of identified converted *S*-wave arrivals. The color version of this figure is available only in the electronic edition.

Summary

The CASIE21-OBS survey is the largest controlled-source wide-angle seismic reflection and refraction experiment conducted off the Cascadia margin to date, and the first of its kind to systematically sample this margin along most of its length, from northern Vancouver Island to southern Oregon. This unique data set is optimal for obtaining seismic V_P and V_S models of the incoming and downgoing Explorer-Juan de Fuca-Gorda plate system and the Cascadia accretionary wedge along 10 trench-crossing 2D profiles, and in some areas for 3D imaging. Our initial assessment indicates that the data are of

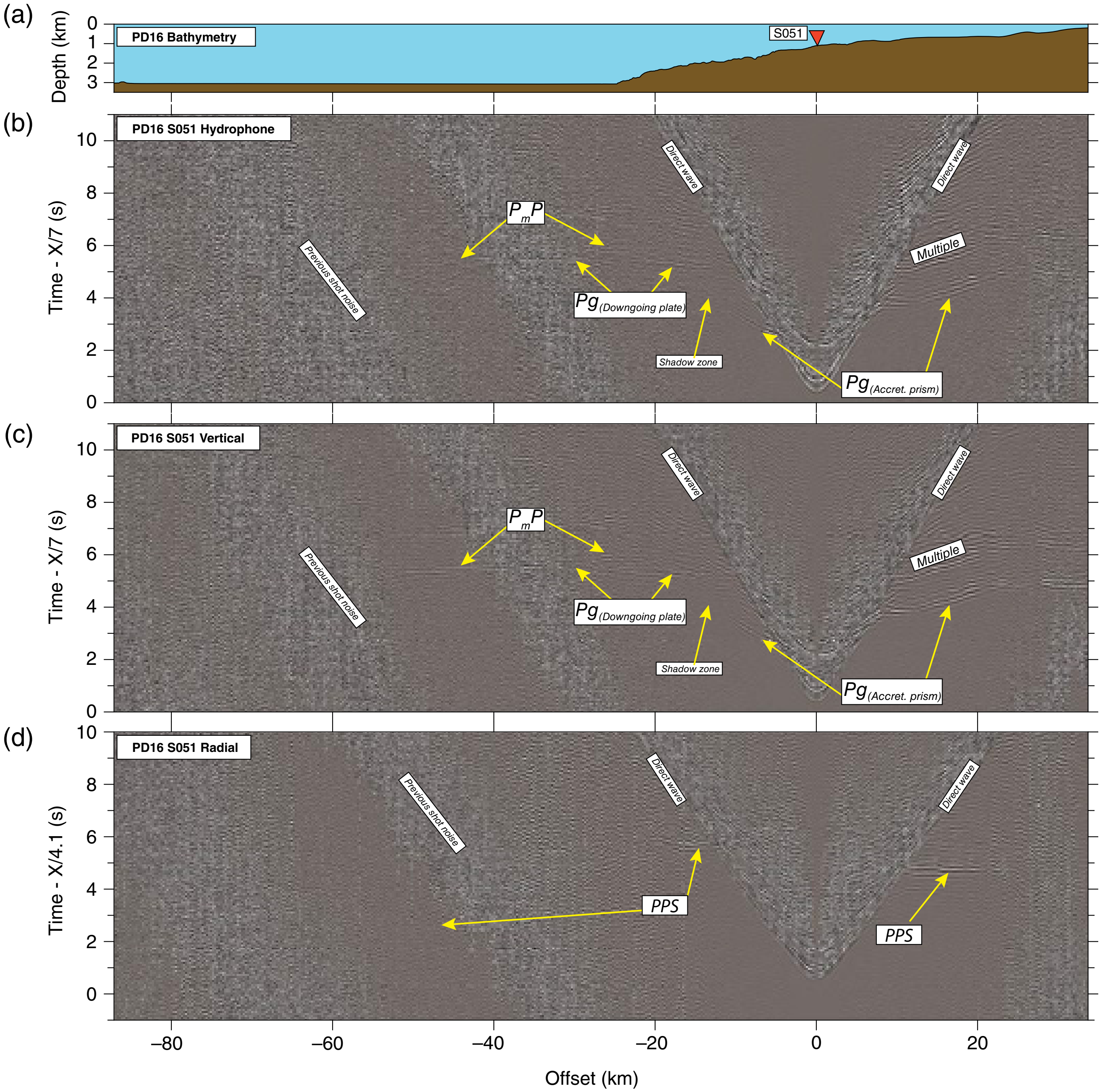

Figure 8. Receiver gathers from instrument S051 located on the upper slope of the accretionary prism on profile PD16 (see location in Fig. 1). Data are band-pass filtered (3–5–20–25 Hz). (a) Bathymetry along profile. (b) Hydrophone channel EDH, with time reduced by 7 km/s. (c) Vertical channel ELZ, with time reduced by 7 km/s. (d) Radial component obtained from rotating horizontal channels EL1 and EL2, with time reduced by 4.1 km/s. Main refracted and reflected phases are labeled. The color version of this figure is available only in the electronic edition.

excellent quality, making them suitable for geophysical investigations using traditional seismic techniques such as travel-time tomography (e.g., Canales *et al.*, 2017; Gase *et al.*, 2021) as well as state-of-the-art methods such as full waveform inversion (Guo *et al.*, 2021, 2022; Jian *et al.*, 2021).

The data are currently being used for investigating hydration of the incoming and downgoing Explorer-Juan de Fuca-Gorda plate system using 2D travel-time tomography (Mann *et al.*, 2022). CASIE21-OBS data set will be open-access and available to the community upon acceptance of this article. The models that researchers will develop from this data set will enable multiple scientific questions of high importance

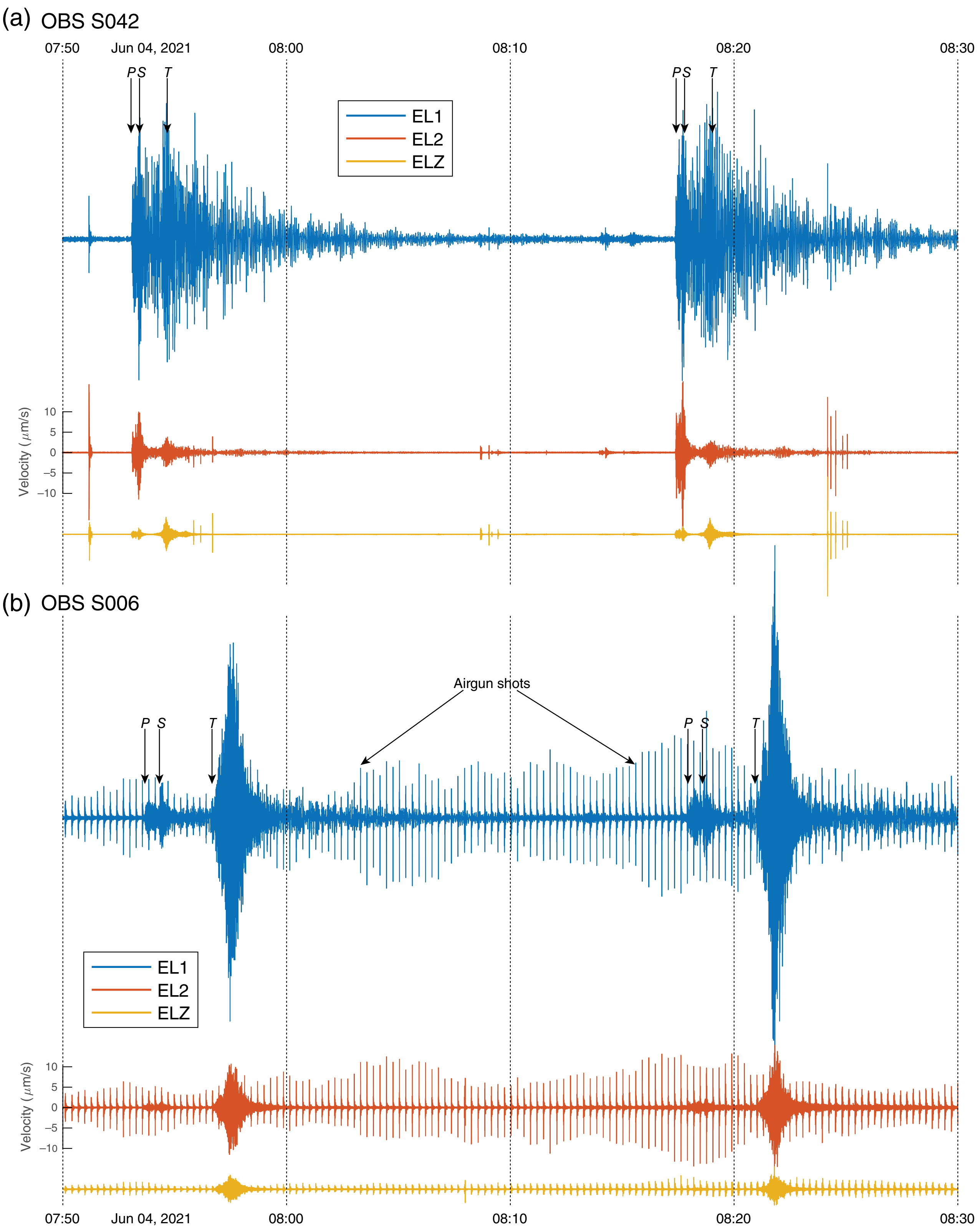

Figure 9. Waveforms of the two 4 June 2021 M_w 5.9 Gorda plate events as recorded in (a) OBS S042 located on line PD19 and (b) OBS S006 located on line PD10. See location of events and instruments in Figure 1. Data are unfiltered and have been corrected for instrument response. Vertical scale is the same for all channels. The color version of this figure is available only in the electronic edition.

to be addressed by, for example: (1) documenting variations in accretionary wedge earthquake shaking properties; (2) modeling the crustal and mantle seismic structure and extent of alteration of the incoming and downgoing plates, and their variability along the margin; and (3) determining accretionary wedge sediment properties such as V_P, V_S, density, porosity, and fluid pore pressure.

Data and Resources

The supplemental material includes tables and figures describing cruise MGL2104 airgun volume changes (Table S1), ocean-bottom seismometer (OBS) site information (Table S2), profile information (Table S3), SEG-Y trace headers (Table S4), and data gaps in miniSEED segments (Table S5, Fig. S1). The CAscadia Seismic Imaging Experiment 2021 ocean-bottom seismometer (CASIE21-OBS) data set is archived and available at the Incorporated Research Institutions for Seismology Data Management Center (IRIS-DMC; Canales *et al.*, 2021): doi: 10.7914/SN/YR_2021. Continuous time series in miniSEED have assigned network code YR_2021 (https://ds.iris.edu/mda/YR_2021). Assembled data in SEG-Y format have assigned identifier 21-008 (https://ds.iris.edu/mda/21-008/). Details on airgun operations are included in Carbotte *et al.* (2021) and multichannel seismic (MCS) data are archived and available at the Marine Geoscience Data System (MGDS): shot data, doi: 10.26022/IEDA/330905 (Carbotte, Boston, and Han, 2022); shot-time files, doi: 10.26022/IEDA/330901 (Carbotte, Han, and Boston,2022). All websites were last accessed in May 2023.

Declaration of Competing Interests

The authors acknowledge that there are no conflicts of interest recorded.

Acknowledgments

The CAscadia Seismic Imaging Experiment 2021 ocean-bottom seismometer (CASIE21-OBS) project was funded by the National Science Foundation (NSF) Award OCE-1929545 to J. P. Canales, N. C. Miller, and D. Lizarralde, and by the U.S. Geological Survey (USGS) Subduction Zone Marine Geohazards Project. The CASIE21-MCS project was funded by NSF Awards OCE-1827452 to S. M. Carbotte, OCE-1827363 to S. Han, and OCE-1829113 to J. P. Canales. Instrumentation was provided and operated by the Ocean-Bottom Seismic Instrument Center (OBSIC) and Scripps Institution of Oceanography (SIO). The authors thank the OBSIC and SIO personnel for their efforts, assistance, and contributions during cruises MGL2103 and OC1206A. The authors thank Holly Smith, NSF's Environmental Compliance Officer, and Sean Higgins, Director of Marine Operations at the Lamont–Doherty Earth Observatory (LDEO), for leading and guiding the Principal Investigators (PIs) through the complex permitting process. Research operations during cruises MGL2103, MGL2104, OC2105A, and OC2106A were conducted under Incidental Harassment Authorization from the National Oceanic and Atmospheric Administration (NOAA)'s National Marine Fisheries Services, NOAA's permit to conduct OBS deployments within the Olympic Coast National Marine Sanctuary, and authorization from Canada Department of Foreign Affairs, Trade and Development (Defense and Security Relations Division) to conduct marine scientific research in areas under Canadian jurisdiction. The authors are grateful to the Quinault Indian Nation for granting them permission to conduct scientific research operations within tribal fishing grounds. The authors thank Scott McMullen, Chairman of the Oregon's Fishermen's Cable Committee, for helping to distribute information about these projects to the Pacific Northwest fishing communities. The authors thank the operator (University of Washington) and crew of the *R/V Rachel Carson* for serving as look-ahead vessel in support of Protected Species Observers during cruise MGL2104. The authors thank the operators of *R/V M.G. Langseth* (Office of Marine Operations at LDEO) and *R/V Oceanus* (Sea Operations at Oregon State University), and science parties, OBSIC and ships' technical personnel, and crews of cruises MGL2103, MGL2104, OC2105A, and OC2106A for their hard work at sea and during precruise preparations to overcome the challenges of conducting sea-going research during the COVID-19 pandemic. The authors thank Janet Watt and an anonymous reviewer for their comments and suggestions that helped them improve the manuscript.

Any use of trade, firm, or product name is for descriptive purposes only and does not imply endorsement by the U.S. Government.

References

Adam, J., D. Klaeschen, N. Kukowski, and E. R. Flueh (2004). Upward delamination of Cascadia Basin sediment infill with landward frontal accretion thrusting caused by rapid glacial age material flux, *Tectonics* **23,** TC3009, doi: 10.1029/2002TC001475.

Alongi, T., S. Y. Schwartz, H. R. Shaddox, and D. T. Small (2021). Probing the Southern Cascadia plate interface with the dense amphibious Cascadia initiative seismic array, *J. Geophys. Res.* **126,** e2021JB022180, doi: 10.1029/2021JB022180.

Anderson, P. N., F. K. Duennebier, and R. K. Cessaro (1987). Ocean borehole horizontal seismic sensor orientation determined from explosive charges, *J. Geophys. Res.* **92,** 3573–3579.

Atwater, B. F. (1987). Evidence for great Holocene earthquakes along the outer coast of Washington State, *Science* **236,** 942–944.

Baumberger, T., R. W. Embley, S. G. Merle, M. D. Lilley, N. A. Raineault, and J. E. Lupton (2018). Mantle-derived helium and multiple methane sources in gas bubbles of cold seeps along the Cascadia continental margin, *Geochem. Geophys. Geosys.* **19,** doi: 10.1029/2018GC007859.

Boulahanis, B., S. M. Carbotte, J. P. Canales, S. Han, and M. R. Nedimović (2022). Structure and evolution of northern Juan de Fuca crust and uppermost mantle over the last 8 Ma from an active-source seismic tomography study, *J. Geophys. Res.* doi: 10.1029/2022JB023987.

Brudzinski, M. R., and R. M. Allen (2007). Segmentation in episodic tremor and slip all along Cascadia, *Geology* **35,** 907–910.

Canales, J. P., S. M. Carbotte, M. R. Nedimović, and H. Carton (2017). Dry Juan de Fuca slab revealed by quantification of water entering Cascadia subduction zone, *Nature Geosci.* **10,** 864–870, doi: 10.1038/ngeo3050.

Canales, J. P., N. C. Miller, W. Baldwin, S. M. Carbotte, S. Han, B. Boston, and D. Lizarralde (2021). CASIE21-OBS: An open-access, OBS controlled-source seismic dataset across the Cascadia accretionary wedge [Data set], *International Federation of Digital Seismograph Networks*, doi: 10.7914/SN/YR_2021.

Carbotte, S. M., B. Boston, and S. Han (2022). Multi-channel seismic shot data from the Cascadia margin acquired during Langseth cruise MGL2104 (2021), doi: 10.26022/IEDA/330905.

Carbotte, S. M., S. Han, and B. Boston (2021). Cascadia seismic imaging experiment—CASIE 21 R/V Marcus G Langseth, *MGL2104 Cruise Rept.* 31 pp.

Carbotte, S. M., S. Han, and B. Boston (2022). Processed seismic navigation data (P1 format) from the Cascadia margin acquired during Langseth cruise MGL2104 (2021), doi: 10.26022/IEDA/330901.

Casey, R., M. E. Templeton, G. Sharer, L. Keyson, B. R. Weertman, and T. Ahern (2018). Assuring the quality of IRIS data with MUSTANG, *Seismol. Res. Lett.* **89,** 630–639, doi: 10.1785/0220170191.

Chester, F. M., C. Rowe, K. Ujiie, J. Kirkpatrick, C. Regalla, F. Remitti, J. C. Moore, V. Toy, M. Wolfson-Schwehr, S. Bose, *et al.* (2013). Structure and composition of the plate-boundary slip zone for the 2011 Tohoku-Oki earthquake, *Science* **342,** 1208–1211, doi: 10.1126/science.1243719.

Christeson, G. L., Y. Nakamura, K. D. McIntosh, and P. L. Stoffa (1996). Effect of shot interval on ocean bottom seismograph and hydrophone data, *Geophys. Res. Lett.* **23,** 3783–3786.

Dash, R., and G. Spence (2011). P-wave and S-wave velocity structure of northern Cascadia margin gas hydrates, *Geophys J. Int.* **187,** 1363–1377, doi: 10.1111/j.1365-246X.2011.05215.x.

Dean, S. M., L. C. McNeill, T. J. Henstock, J. M. Bull, S. P. S. Gulick, J. A. Austin, N. L. B. Bangs, Y. S. Djajadihardja, and H. Permana (2010). Contrasting décollement and prism properties over the Sumatra 2004-2005 earthquake rupture boundary, *Science* **329,** 207–210, doi: 10.1126/science.1189373.

Delph, J. R., A. Levander, and F. Niu (2018). Fluid controls on the heterogeneous seismic characteristics of the Cascadia Margin, *Geophys. Res. Lett.* **45,** 11,021–11,029, doi: 10.1029/2018GL079518.

Doran, A. K., and G. Laske (2017). Ocean-bottom seismometer instrument orientations via automated Rayleigh-wave arrival-angle measurements, *Bull. Seismol. Soc. Am.* **107,** 691–708, doi: 10.1785/0120160165.

Duennebier, F. K., P. N. Anderson, and G. J. Fryer (1987). Azimuth determination of and from horizontal ocean bottom seismic sensors, *J. Geophys. Res.* **92,** 3567–3572.

Flueh, E. R., M. A. Fisher, J. Bialas, J. R. Childs, D. Klaeschen, N. Kukowski, T. Parsons, U. ten Brink, A. M. Tréhu, and N. Vidal (1998). New seismic images of the Cascadia subduction zone from cruise SO108-ORWELL, *Tectonophysics* **293,** 69–84.

Gase, A. C., H. J. A. Van Avendonk, N. L. Bangs, D. Bassett, S. A. Henrys, D. H. N. Barker, S. Kodaira, K. M. Jacobs, T. W. Luckie, D. A. Okaya, *et al.* (2021). Crustal structure of the northern Hikurangi margin, New Zealand: Variable accretion and overthrusting plate strength influenced by rough subduction, *J. Geophys. Res.* **126,** e2020JB021176, doi: 10.1029/2020JB021176.

Geersen, J., L. McNeill, and T. J. Henstock (2013). The 2004 Aceh-Andaman earthquake: Early clay dehydration controls shallow seismic rupture, *Geochem. Geophys. Geosys.* **14,** 3315–3323, doi: 10.1002/ggge.20193.

Gerdom, M., A. M. Trehu, E. R. Flueh, and D. Klaeschen (2000). The continental margin off Oregon from seismic investigations, *Tectonophysics* **329,** 79–97.

Goldfinger, C., S. Galer, J. Beeson, J. Hamilton, T. Hamilton, B. Black, C. Romsos, J. Patton, C. H. Nelson, R. Hausmann, *et al.* (2017). The importance of site selection, sediment supply, and hydrodynamics: A case study of submarine paleoseismology on the northern Cascadia margin, Washington USA, *Mar. Geol.* **384,** 4–46, doi: 10.1016/j.margeo.2016.06.008.

Goldfinger, C., H. C. Nelson, A. E. Morey, J. E. Johnson, J. R. Patton, E. Karabanov, J. Gutiérrez-Pastor, A. T. Eriksson, E. Gràcia, G. Dunhill, *et al.* (2012). Turbidite event history - Methods and implications for Holocene paleoseismicity of the Cascadia subduction zone, in *Earthquake Hazards of the Pacific Northwest Coastal and Marine Regions*, R. Kayen (Editor), *U.S. Geol. Surv. Profess. Pap. 1661-F*, U.S. Geological Survey, Reston, Virginia, 170 pp.

Gomberg, J. (2018). Cascadia onshore-offshore site response, submarine sediment mobilization, and earthquake recurrence, *J. Geophys. Res.* **123,** 1381–1404, doi: 10.1002/2017JB014985.

Gong, J., and J. J. McGuire (2018). Interactions between strike-slip earthquakes and the subduction interface near the Mendocino Triple Junction, *Earth Planet. Sci. Lett.* **482,** 414–422, doi: 10.1016/j.epsl.2017.11.022.

Gulick, S. P. S., J. A. Austin, L. McNeill, N. L. B. Bangs, K. M. Martin, T. J. Henstock, J. M. Bull, S. Dean, Y. S. Djajadihardja, and H. Permana (2011). Updip rupture of the 2004 Sumatra earthquake extended by thick indurated sediments, *Nature Geosci.* **4,** 453–456, doi: 10.1038/NGEO1176.

Gulick, S. P. S., A. M. Meltzer, and S. H. Clarke (1998). Seismic structure of the southern Cascadia subduction zone and accretionary prism north of the Mendocino triple junction, *J. Geophys. Res.* **103,** 27,207–27,222.

Guo, P., S. C. Singh, V. A. Vaddineni, I. Grevemeyer, and E. Saygin (2022). Lower oceanic crust formed by in situ melt crystallization revealed by seismic layering, *Nature Geosci.* **15,** 591–596, doi: 10.1038/s41561-022-00963-w.

Guo, P., S. C. Singh, V. A. Vaddineni, G. Visser, I. Grevemeyer, and E. Saygin (2021). Nonlinear full waveform inversion of wide-aperture OBS data for Moho structure using a trans-dimensional Bayesian method, *Geophys J. Int.* **224,** 1056–1078, doi: 10.1093/gji/ggaa505.

Gutscher, M.-A., D. Klaeschen, E. R. Flueh, and J. Malaivieille (2001). Non-Coulomb wedges, wrong-way thrusting, and natural hazards in Cascadia, *Geology* **29,** 379–382.

Han, S., N. L. Bangs, S. M. Carbotte, D. M. Saffer, and J. C. Gibson (2017). Links between sediment consolidation and Cascadia megathrust slip behaviour, *Nature Geosci.* **10,** 954–959, doi: 10.1038/s41561-017-0007-2.

Han, S., S. M. Carbotte, J. P. Canales, H. Carton, M. R. Nedimović, J. Gibson, and G. Horning (2016). Seismic reflection imaging of the Juan de Fuca plate from ridge to trench; new constraints on the distribution of faulting and evolution of the crust prior to subduction, *J. Geophys. Res.* **121,** 1849–1872, doi: 10.1002/2015JB012416.

Han, S., S. M. Carbotte, J. P. Canales, M. R. Nedimović, and H. Carton (2018). Along-trench structural variations of the subducting Juan de Fuca plate from multichannel seismic reflection imaging, *J. Geophys. Res.* **123,** 3122–3146, doi: 10.1002/2017JB015059.

Heuret, A., C. P. Conrad, R. Funiciello, S. Lallemand, and L. Sandri (2012). Relation between subduction megathrust earthquakes, trench sediment thickness and upper plate strain, *Geophys. Res. Lett.* **39,** L05304, doi: 10.1029/2011GL050712.

Horning, G., J. P. Canales, S. M. Carbotte, S. Han, H. Carton, M. R. Nedimović, and P. E. van Keken (2016). A 2-D tomographic model of the Juan de Fuca plate from accretion at axial seamount to subduction at the Cascadia margin from an active source OBS survey, *J. Geophys. Res.* **121,** 5859–5879, doi: 10.1002/2016JB013228.

Hüpers, A., M. E. Torres, S. Owari, L. C. McNeill, B. Dugan, T. J. Henstock, K. L. Milliken, K. E. Petronotis, J. Backman, S. Bourlange, *et al.* (2017). Release of mineral-bound water prior to subduction tied to shallow seismogenic slip off Sumatra, *Science* **356,** 841–844.

Hyndman, R. D., C. J. Yorath, R. M. Clowes, and E. E. Davis (1990). The northern Cascadia subduction zone at Vancouver Island: Seismic structure and tectonic history, *Can. J. Earth Sci.* **27,** 313–329.

International Federation of Digital Seismograph Networks (FDSN) (2012). SEED reference manual: standard for the exchange of earthquake data. SEED format version 2.4, *International Federation of Digital Seismograph Networks*, Published by the Incorporated Research Institutions for Seismology (IRIS), 224 pp.

Janiszewski, H. A., and G. A. Abers (2015). Imaging the plate interface in the Cascadia seismogenic zone: New constraints from offshore receiver functions, *Seismol. Res. Lett.* **86,** 1261–1269, doi: 10.1785/0220150104.

Jian, H., M. R. Nedimović, J. P. Canales, and K. W. H. Lau (2021). New insights into the rift to drift transition across the northeastern Nova Scotian margin from wide-angle seismic waveform inversion and reflection imaging, *J. Geophys. Res.* **126,** e2021JB022201, doi: 10.1029/2021JB022201.

Johnson, H. P., J. S. Gomberg, S. L. Hautala, and M. S. Salmi (2017). Sediment gravity flows triggered by remotely generated earthquake waves, *J. Geophys. Res.* **122,** 4584–4600, doi: 10.1002/2016JB013689.

Johnson, H. P., S. Merle, M. Salmi, R. Embley, E. Sampaga, and M. Lee (2019). Anomalous concentration of methane emissions at the continental shelf edge of the Northern Cascadia Margin, *J. Geophys. Res.* **124,** doi: 10.1029/2018JB016453.

Johnson, J. E., C. Goldfinger, A. M. Trehu, N. L. B. Bangs, M. E. Torres, and J. Chevallier (2006). North-south variability in the history of deformation and fluid venting across Hydrate Ridge, Cascadia Margin, A. M. Trehu, G. Bohrmann, M. E. Torres, and F. S. Colwell (Editors), *Proc. of the ODP Sci. Results*, Ocean Drilling Program, College Station, Texas, 1–29.

Kumar, D., M. K. Sen, and N. L. Bangs (2007). Gas hydrate concentration and characteristics within Hydrate Ridge inferred from multicomponent seismic reflection data, *J. Geophys. Res.* **112,** doi: 10.1029/2007JB004993.

MacKay, M. E. (1995). Structural variation and landward vergence at the toe of the Oregon prism, *Tectonics* **14,** 1309–1320.

Mann, M. E., J. P. Canales, H. Jian, N. C. Miller, S. M. Carbotte, S. Han, B. Boston, and J. Beeson (2022). Initial active-source Vp tomography results for CASIE21 experiment line PD12 offshore northwestern Oregon, and a comparison with nearby land-based receiver functions, *Abstract S46B-02 presented at 2022 Fall Meeting, AGU*, Chicago, Illinois, 12–16 December.

McCrory, P. A., J. L. Blair, F. Waldhauser, and D. H. Oppenheimer (2012). Juan de Fuca slab geometry and its relation to Wadati-Benioff zone seismicity, *J. Geophys. Res.* **117,** no. B9, doi: 10.1029/2012JB009407.

McCrory, P. A., J. E. Constantz, A. G. Hunt, and J. L. Blair (2016). Helium as a tracer for fluids released from the Juan de Fuca lithosphere beneath the Cascade forearc, *Geochem. Geophys. Geosys.* doi: 10.1002/2015GC006198.

Moreno, M., C. Haberland, O. Oncken, A. Rietbrock, S. Angiboust, and O. Heidbach (2014). Locking of the Chile subduction zone controlled by fluids pressure before the 2010 earthquake, *Nature Geosci.* **7,** 292–296.

Morton, E. A., S. L. Bilek, and C. A. Rowe (2018). Newly detected earthquakes in the Cascadia subduction zone linked to seamount subduction and deformed upper plate, *Geology* **46,** 943–946, doi: 10.1130/G45354.1.

Nakamura, Y., P. L. Donoho, P. H. Roper, and P. M. McPherson (1987). Large-offset seismic surveying using ocean-bottom seismographs and air guns: Instrumentation and field technique, *Geophysics* **52,** 1601–1611.

Nedimović, M. R., D. R. Bohnenstiehl, S. M. Carbotte, J. P. Canales, and R. P. Dziak (2009). Faulting and hydration of the Juan de Fuca Plate system, *Earth Planet. Sci. Lett.* **284,** 94–102.

Parsons, T., A. M. Trehu, J. H. Luetgert, K. Miller, F. Kilbride, R. E. Wells, M. A. Fisher, E. R. Flueh, U. ten Brink, and N. I. Christensen (1998). A new view into the Cascadia subduction zone and volcanic arc: Implications for earthquake hazards along the Washington margin, *Geology* **26,** 199–202.

Peacock, S., G. K. Westbrook, and G. Bais (2010). S-wave velocities and anisotropy in sediments entering the Nankai subduction zone, offshore Japan, *Geophys J. Int.* **180,** 743–758.

Peterson, J. R. (1993). Observations and modeling of seismic background noise, *U.S. Geol. Surv. Open-File Rept. 93-322*, doi: 10.3133/ofr93322.

Peterson, D. E., and K. M. Keranen (2019). A high wave speed basal sedimentary layer identified from seismic imaging of the plate boundary in central Cascadia, *J. Geophys. Res.* **124,** doi: 10.1029/2018jb017227.

Pitcher, B. W., and A. J. R. Kent (2019). Statistics and segmentation: Using Big data to assess cascades arc compositional variability, *Geochim. Cosmochim. Acta* **265,** 443–467, doi: 10.1016/j.gca.2019.08.035.

Poli, P., A. Maksymowicz, and S. Ruiz (2017). The Mw8.3 Illapel earthquake (Chile): Preseismic and postseismic activity associated with hydrated slab structures, *Geology* **45,** 247–250.

Priest, G. R., R. C. Witter, Y. J. Zhang, C. Goldfinger, K. Wang, and J. C. Allan (2017). New constraints on coseismic slip during southern Cascadia subduction zone earthquakes over the past 4600 years implied by tsunami deposits and marine turbidites, *Nat. Hazards* **88,** 285–313, doi: 10.1007/s11069-017-2864-9.

Russell, J. B., Z. Eilon, and S. G. Mosher (2019). OBSrange: A new tool for the precise remote location of ocean-bottom seismometers, *Seismol. Res. Lett.* **90,** 1627–1641, doi: 10.1785/0220180336.

Schmalzle, G. M., R. McCaffrey, and K. C. Creager (2014). Central Cascadia subduction zone creep, *Geochem. Geophys. Geosys.* **15,** doi: 10.1002/2013GC005172.

Schmidt, M. E., A. L. Grunder, and M. C. Rowe (2008). Segmentation of the Cascade Arc as indicated by Sr and Nd isotopic variation among diverse primitive basalts, *Earth Planet. Sci. Lett.* **266,** 166–181.

Scholl, D. W., S. H. Kirby, R. von Huene, H. Ryan, R. E. Wells, and E. L. Geist (2015). Great (>=Mw8.0) megathrust earthquakes and the subduction of excess sediment and bathymetrically smooth seafloor, *Geosphere* **11,** 236–265, doi: 10.1130/GES01079.1.

Seno, T. (2017). Subducted sediment thickness and Mw 9 earthquakes, *J. Geophys. Res.* **122,** doi: 10.1002/2016JB013048.

Shillington, D. J., A. Bécel, M. R. Nedimović, H. Kuehn, S. C. Webb, G. A. Abers, K. M. Keranen, J. Li, M. Delescluse, and G. A. Mattei-Salicrup (2015). Link between plate fabric, hydration and subduction zone seismicity in Alaska, *Nature Geosci.* **8,** 961–964.

Stachnik, J. C., A. F. Sheehan, D. W. Zietlow, Z. Yang, J. Collins, and A. Ferris (2012). Determination of New Zealand ocean bottom seismometer orientation via Rayleigh-wave polarization, *Seismol. Res. Lett.* **83,** 704–713, doi: 10.1785/0220110128.

Stone, I., J. E. Vidale, S. Han, and E. Roland (2018). Catalog of offshore seismicity in Cascadia: Insights into the regional distribution of microseismicity and its relation to subduction processes, *J. Geophys. Res.* doi: 10.1002/2017JB014966.

Trabattoni, A., G. Barruol, R. Dreo, A. O. Boudraa, and F. R. Fontaine (2020). Orienting and locating ocean-bottom seismometers from ship noise analysis, *Geophys J. Int.* **220,** 1774–1790, doi: 10.1093/gji/ggz519.

Tréhu, A. M., R. J. Blakely, and M. C. Williams (2012). Subducted seamounts and recent earthquakes beneath the central Cascadia forearc, *Geology* **40,** 103–106.

Tsuji, T., J. Dvorkin, G. Mavko, N. Nakata, T. Matsuoka, A. Nakanishi, S. Kodaira, and O. Nishizawa (2011). Vp/Vs ratio and shear-wave splitting in the Nankai Trough seismogenic zone: Insights into effective stress, pore pressure, and sediment consolidation, *Geophysics* **76,** WA71–WA82, doi: 10.1190/1.3560018.

van Rijsingen, E., S. Lallemand, M. Peyret, D. Arcay, A. Heuret, F. Funiciello, and F. Corbi (2018). How subduction interface roughness influences the occurrence of large interplate earthquakes, *Geochem. Geophys. Geosys.* **19,** doi: 10.1029/2018GC007618.

VanderBeek, B. P., and D. R. Toomey (2019). Pn tomography of the Juan de Fuca and Gorda plates: Implications for mantle deformation and hydration in the oceanic lithosphere, *J. Geophys. Res.* **124,** 8565–8583, doi: 10.1029/2019JB017707.

Vannucchi, P., E. Spagnuolo, S. Aretusini, G. Di Toro, K. Ujiie, A. Tsutsumi, and S. Nielsen (2017). Past seismic slip-to-trench recorded in Central America megathrust, *Nature Geosci.* **10,** 935–940, doi: 10.1038/s41561-017-0013-4.

Wada, I., and K. Wang (2009). Common depth of slab-mantle decoupling: Reconciling diversity and uniformity of subduction zones, *Geochem. Geophys. Geosys.* **10,** Q10009, doi: 10.1029/2009GC002570.

Walton, M. A. L., L. M. Staisch, T. Dura, J. K. Pearl, B. Sherrod, J. Gomberg, S. Engelhart, A. Tréhu, J. Watt, J. Perkins, *et al.* (2021). Toward an Integrative geological and geophysical view of Cascadia subduction zone earthquakes, *Annu. Rev. Earth Planet. Sci.* **49,** 367–398, doi: 10.1146/annurev-earth-071620-065605.

Ward, K. M., and A. M. Tréhu (2020). Complementing the 2020 Langseth offshore Cascadia survey with a large-N onshore nodal deployment [Data set], *International Federation of Digital Seismograph Networks*, doi: 10.7914/SN/Z4_2020.

Watt, J. T., and D. S. Brothers (2020). Systematic characterization of morphotectonic variability along the Cascadia convergent margin: Implications for shallow megathrust behavior and tsunami hazards, *Geosphere* **17,** 95–117, doi: 10.1130/ges02178.1.

Webb, S. C. (1998). Broadband seismology and noise under the ocean, *Rev. Geophys.* **36,** 105–142.

Wech, A. G. (2010). Interactive tremor monitoring, *Seismol. Res. Lett.* **81,** 664–669, doi: 10.1785/gssrl.81.4.664.

Wilson, D. S. (2002). The Juan de Fuca Plate and slab - Isochron structure and Cenozoic plate motions, in *The Cascadia Subduction Zone and Related Subduction Systems. Seismic Structure, Intraslab Earthquakes and Processes, and Earthquake Hazards*, S. Kirby, K. Wang, and S. Dunlop (Editors), *U.S. Geol. Survey Open-File Rept. 02-328*, U.S. Geological Survey, Reston, Virginia, 9–12 pp.

Yelisetti, S., G. D. Spence, M. Scherwath, M. Riedel, and D. Klaeschen (2017). Dual-vergence structure from multiple migration of widely spaced OBSs, *Tectonophysics* **718,** 45–60, doi: 10.1016/j.tecto.2017.04.005.

Zha, Y., S. C. Webb, and W. Menke (2013). Determining the orientations of ocean bottom seismometers using ambient noise correlation, *Geophys. Res. Lett.* **40,** 3585–3590, doi: 10.1002/grl.50698.

Zhu, J., J. P. Canales, S. Han, S. M. Carbotte, A. F. Arnulf, and M. R. Nedimović (2020). Vp/Vs ratio of incoming sediments off Cascadia Subduction Zone from analysis of controlled-source multi-component OBS records, *J. Geophys. Res.* doi: 10.1029/2019JB019239.

Manuscript received 18 January 2023
Published online 23 May 2023